Automated Microcontact Bioprinting for High-Throughput Manufacturing of Lubricant-Infused Microarrays

Lubna Najm[a], Amid Shakeri[b*], Liane Ladouceur[c], Samantha Dacalos[d], Sakina Hussain[d], Inaam Chattha[d], Hareet Sidhu[d], Tohid F. Didar[*a, c, e]

[a] School of Biomedical Engineering, McMaster University, 1280 Main Street West, Hamilton, Ontario L8S 4L8, Canada

[b] Institute of Biomaterials Engineering, University of Toronto, Toronto, Ontario, M5S 3G9; Canada

[c] Department of Mechanical Engineering, McMaster University, 1280 Main Street West, Hamilton, Ontario L8S 4L7, Canada

[d] Department of Biochemistry and Biomedical Sciences, McMaster University, 1280 Main Street West, Hamilton, Ontario L8S 4K1, Canada

[e] Institute for Infectious Disease Research (IIDR), 1280 Main St W, McMaster University, Hamilton, Ontario, Canada, L8S 4L8

* Address correspondence to didart@mcmaster.ca and amid.shakeri@utoronto.ca

Microarrays are widely used for detecting target analytes and biomarkers, with fabrication methods ranging from non-contact to contact bioprinting techniques. Microcontact bioprinting (μCP), which utilizes elastomeric stamps to transfer biorecognition molecules (bioinks) onto substrates, offers advantages such as customizability, cost-effectiveness, and versatility in handling bioinks with high viscosities. Despite its prevalent use in laboratory settings, μCP faces challenges in achieving the repeatability and reproducibility required for industrial manufacturing. In this study, we address these limitations by developing and optimizing a μCP protocol using industrial techniques. A key innovation in our approach is the combination of microcontact printing with fluorosilanization, enabling the use of lubricant-infused surfaces to prevent non-specific attachment. Additionally, we enhance biomolecule immobilization through covalent attachment using a modified bioink formulation. We identify and mitigate high-risk failure modes including bioink formulation, application and removal, environmental conditions, and force application during stamping. Furthermore, we integrate an automated syringe pump and a standardized force application system, taking critical steps toward industrial scalability. Using lubricant-infused substrates, our optimized μCP protocol demonstrates significant improvements in repeatability and reproducibility, achieving intra-assay and inter-assay coefficients of variance below 10% and signal-to-noise ratios exceeding 15. These advancements validate our μCP method for high-throughput, scalable microarray fabrication, paving the way for its implementation in industrial manufacturing.

Key Words: microcontact bioprinting, microarrays, lubricant infused surfaces, failure mode and effects analysis, automation

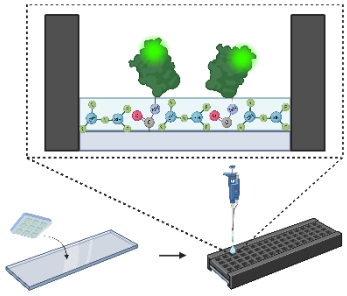

Microarrays are commonly used in literature, for their ease-of-integration within established biological and immunofluorescence assays (IFAs), the most common being sandwich enzyme-linked immunosorbent assays (ELISAs).[1] By combining microarrays and IFAs, target analytes and biomarkers are distinguishable, enhancing their applicability for diagnosing and monitoring disease in clinical and industrial settings. [2–11] A variety of fabrication methods, including both non-contact and contact bioprinting techniques, are available for creating microarrays.[10,12–15]

Non-contact bioprinting techniques, such as piezoelectric, continuous inkjet, and drop-on-demand printing, offer the advantage of precise, high-speed deposition of bioinks onto substrates without direct contact.[12,16–19] These methods are highly automated and suitable for large-scale production; however, they often face limitations when printing highly viscous bioinks or large biomolecules due to issues like nozzle clogging and reduced resolution. Additionally, non-contact systems can struggle to customize microarrays with intricate features, particularly when unique or complex patterns are required.[16,17,20] In contrast, microcontact bioprinting (μCP), directly transfer bioinks from a patterned stamp onto the substrate, allowing for greater flexibility in feature design. μCPs can handle a wider range of bioink viscosities, including large and complex biomolecules, and offer enhanced customizability in terms of pattern geometry. [21,22] However, contact bioprinting can face challenges with scalability and consistency in industrial settings due to the manual nature of the process.[23,24]

μCP involves the fabrication of a stamp with micron features made from elastomers that are flexible, affordable, and easily accessible. The micron features are cast utilizing a silicon mold and can be predesigned with unique and fine detailed patterns and microarrays.[8,25–29] μCP involves the application of a bioink across the featured stamp surface, followed by physical force for direct biomolecule transfer onto substrates.[8,21,23,26][30] The dimensions of the stamps allow microcontact printing to cover a wide surface area upon a single print, making it faster than non-contact methods such as pin or stencil printing, which often require multiple passes to print large areas. [23,25]

Traditionally, microcontact printing has two main limitations. It typically relies on the physical attachment of biomolecules to the surface, which reduces the robustness of the resulting microarrays. The introduction of cross-linking agents within the bioink to induce covalent attachment as well as additives to control fluid evaporation rates can be investigated in μCP for microarray development.[23,26,30,31] Furthermore, the PDMS stamps used in the process can leave behind residue, leading to non-specific attachment and ultimately reducing the sensitivity in bioassays. μCP also has challenges in scalability for industry translation and is predominantly used in lab scale settings. This is mainly due to the lack of characterization and assessment of factors affecting the repeatability and reproducibility of μCP microarrays, resulting in low signal-to-noise ratios (SNRs) and high percentage coefficients of variance. [12,21] [32–38]

We propose a fully characterized μCP protocol for repeatability and reproducibility. We developed a bioink formulation that enables covalent binding of biomolecules to the surface during microcontact printing. Additionally, we established a protocol that combines microcontact printing with fluorosilanization (FS) treatment to create a lubricant-infused surface, effectively preventing non-specific attachment. By exploring the role of surface interactions and covalent binding in biomolecule immobilization and optimizing the impact of external factors on the μCP process, we

achieved SNRs exceeding 15, along with intra-assay and inter-assay %CVs below 10%. To address scalability and industrial translation, we present a proof-of-concept design that standardizes the μCP procedure, marking a significant step towards full automation for integration into industrial manufacturing lines.

Results and Discussion

Stamp Fabrication, Substrate Functionalization, and Bioprinting Protocol

In creating the stamp mold, micron scale, square pillar features were etched into a silicon wafer through soft photolithography. Square pillars were chosen as the feature design of the stamps due to their ease of fabrication and image analysis. The square pillars with the dimensions of 150μm × 150μm × 1μm were spaced equally apart by 150μm (**Figure 1d**). Polydimethylsiloxane (PDMS) at the ratio of 10:1, base: curing agent, was cast on the fabricated mold to create flexible stamps for microcontact printing. PDMS, upon solidification, becomes a flexible elastomer with intermediate liquid absorption characteristics, making it ideal for absorbing bioink and facilitating bioink transfer onto functionalized substrates. [25,39–43]. Each stamp has a dimension of 2cm × 1.8cm × 0.3cm.

Poly (methyl methacrylate) (PMMA) were used as substrates in microcontact printing to ensure the cost-effectiveness for industry scale usability.[44] The substrates were first functionalized with CO_2 plasma treatment, depositing activated carboxyl groups and rendering the substrates hydrophilic to ensure maximal bioink transfer. [8,43,45–55] The initial contact angle (CA) of untreated PMMA was 66.03°, indicating a relatively hydrophobic surface. By performing CO_2 plasma treatment, for 3min to 15min, the CAs significant decreased to 55.7º to 38.9º, respectively, making the substrate sufficiently hydrophilic for μCP. Extending the plasma treatment to 30min caused the contact angle to drop further to 19.9°. We realized that this prolonged treatment resulted in over-etching, damaging the already formed carboxyl groups and ultimately reducing the effectiveness of covalent attachment during microcontact printing.[56,57] Therefore, 15min plasma treatment was chosen as the optimum time to provide a degree of hydrophilicity while ensuring activated carboxyl groups remain on the functionalized PMMA substrates (**Figure 1b**).

To induce covalent crosslinking through μCP, we use 1-Ethyl-3-(3-dimethylaminopropyl) carbodiimide/N-Hydroxysuccinimide (EDC/NHS) along with the biomolecule of interest in the bioink formulation. The bioink was first applied on the PDMS stamps in the form of 5μL droplets. The droplets were incubated on the stamp's square pillar features, allowing bioink to get absorbed into the material of each feature (**Figure 1a**). After incubation, removal of excess volume and subsequent air drying was conducted, allowing for evaporation of the bioink (Figure 1a). The elastomeric stamp was then placed onto the functionalized PMMA substrate. Force was applied onto the stamp for physical transfer of the bioink from the stamp features onto the substrate, facilitating biomolecule immobilization.

To illustrate the efficacy of μCP in each step, we utilized bovine serum albumin-fluorescein isothiocyanate (BSA-FITC) as the desired biomolecule in our bioink and measured the

fluorescence signal of the patterns and background (noise) after printing. The results were indicated as SNRs for comparing different conditions. When comparing short and long incubation times after adding the bioink droplets onto the stamps, 2min droplet incubation showed significantly higher SNR value compared to a longer incubation of 30min. Thus, 2min was sufficient for bioink absorption (**Figure S1**).

The PDMS stamps also showed durability and reusability, making them effective for up to 10 consecutive prints before needing to be replaced, referred to as 'aged stamps' (**Figure S2**) To increase the efficiency of μCP, we tested different stamp treatment methods to prevent transferring PDMS residue and optimize the surface energy of the stamp. After evaluating fluorosilane (FS) treatment using chemical vapor deposition (CVD) [8,31,45,46,58,59], and (3-Aminopropyl) triethoxysilane (APTES) treatment,[60] the untreated stamps proved to have better functionality and significantly higher SNRs (**Figure 1c**). The associated fluorescence images for untreated stamps compared to aged, FS treated, and APTES treated stamps are shown in **Figure S3**.

After μCP, the printed substrates were fluorosilanized using CVD followed by superstructure assembly and the introduction of perfuoroperhydrophenanthrene (PFPP) lubricant (**Figure 1e**).[8,45,46,51,59] The lubricant-infused surface (LIS) was leveraged as a blocking strategy for the microarray as it showed enhanced SNRs and reduced background noise when biotinylated monoclonal antibodies or bovine serum albumin-fluorescein isothiocyanate (BSA-FITC), were covalently microcontact printed (**Figure 1f**). To assess the functionality of the lubricant-infused microarray as a blocking agent for SNR enhancement, biotinylated monoclonal detector antibodies (DAb) for interleukin-6 (IL-6) and tumor necrosis factor receptor 1 (TNF R1) were printed separately, with one set of wells containing PFPP lubricant layer and one set of wells without lubricant. These were compared to a control of only PFPP, and streptavidin cyanine-5 (Cy5) was used for fluorescence detection. As shown in **Figure 1g**, the SNRs of both lubricant-infused antibody microarrays significantly increased compared to standard microarrays without lubricant, at $P<0.1$ and $P<0.0001$ in the cases of IL-6 DAb and TNF R1 DAb, respectively.

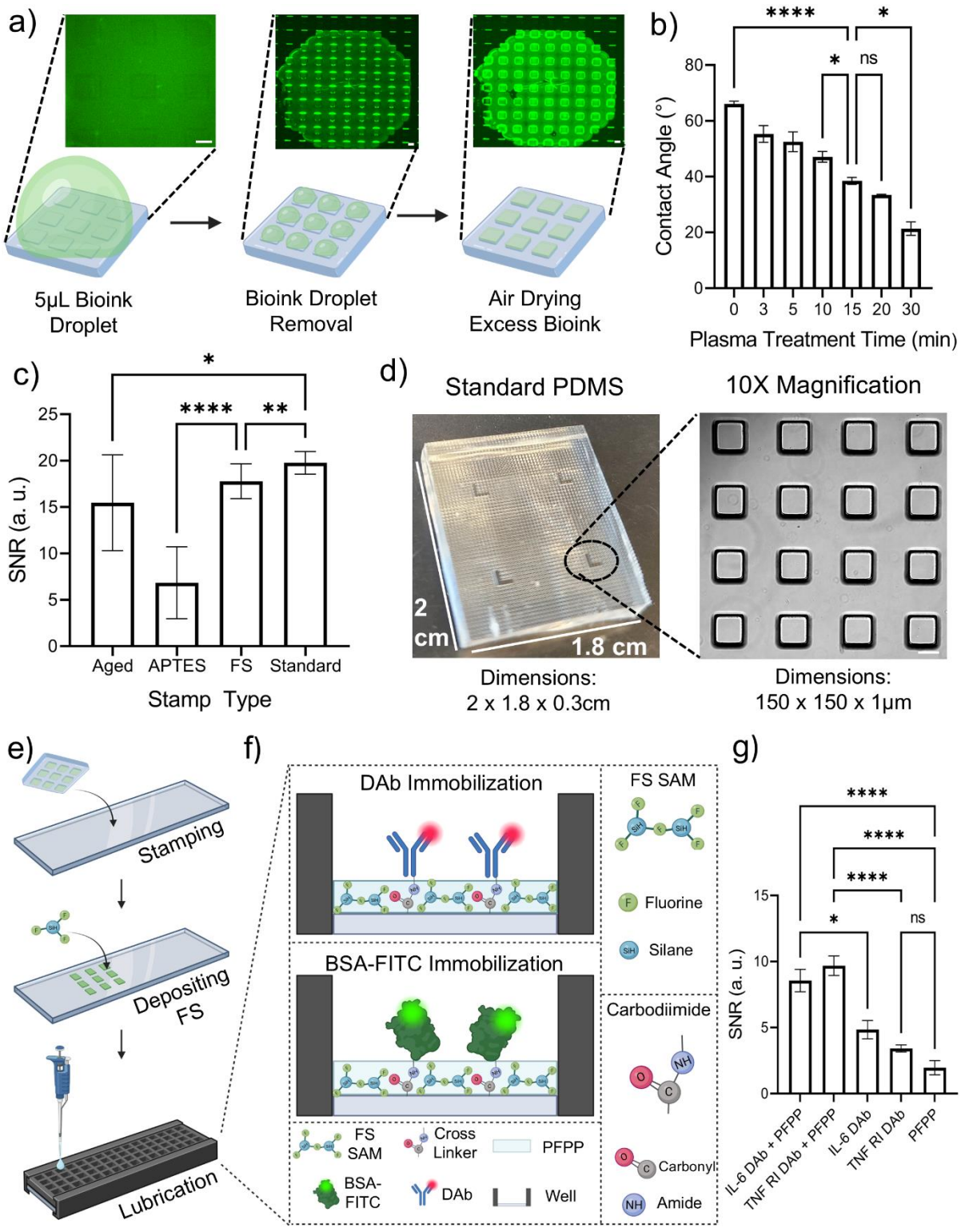

Figure 1. Overview of µCP protocol, stamp fabrication and surface lubrication. A) Depicts the application of a 5µL bioink droplet, followed by droplet removal and air drying to remove excess bioink, with associated fluorescence images. Scale bars were 100 µm. **B)** Depicts contact angle measurements as CO_2 plasma treatment time increases. **C)** SNRs after µCP with aged, APTES-treated, FS-treated and standard stamps. **D)** Dimensions of the PDMS stamps and

individual features, imaged *via* brightfield microscopy. Scale bars were 100 µm. **E)** Depicts the post-stamping FS-treatment, superstructure application, and lubrication of printed PMMA substrates. **F)** Depicts the immobilization of DAb and BSA-FITC, with carbodiimide crosslinking, as well as blocking mechanisms induced by FS and PFPP SAMs. Error bars calculated using the mean of standard deviation for all data. **G)** SNRs after µCP IL-6 and TNF RI DAb with and without PFPP lubrication, compared to control of just PFPP lubricant. Error bars calculated using standard error of the mean.

The repeatability of the µCP protocol was for achieving industry standards in device manufacturing. Failure Mode and Effects Analysis (FMEA) was conducted for each of the µCP steps, assessing the possibility of failure modes that could occur within our protocol.[8,61–65] The steps within our protocol deemed to have highest risk priority number (RPN) based on the product of severity (SEV), frequency of occurrence (OCC), and detectability of failure (DET), were as follows: 1) plasma treatment procedure (risk priority number (RPN) = 70); 2) the formulation of the bioink (RPN = 140); 3) the droplet removal process (RPN = 280); 4) the conditions during airdrying (RPN = 392); and 5) force application (RPN = 128) (**Table S1)**. These five steps were then addressed and optimized in the bioprinting of BSA-FITC, for enhancing repeatability and reproducibility of microarrays using µCP.

Optimization of Bioink Formulation

The first high-risk step determined by FMEA was the optimization of the bioink formulation. Without covalent attachment, and only relying on physical biomolecule transfer, the immobilization was not strong enough to withstand washing stages necessary after lubrication (**Figure S4**). Compared to conditions where no crosslinking agent was present or only EDC was included in the bioink, we observed enhanced SNRs when both EDC and NHS were incorporated. As opposed to the O-acylisourea intermediate formed by EDC, the NHS ester offers greater stability, which facilitates more efficient binding to the primary amines of biomolecules (**Figure S5**). The ratio of EDC to NHS necessary for effective conjugation into a crosslinking complex showed optimal values of 5mg EDC to 3mg NHS (**Figure S6** and **Figure S7**). Furthermore, the concentration of BSA-FITC, as the biomolecule of interest for printing, was optimized to 200µg/mL resulting in the highest SNR (**Figure S8**).

The ratios of EDC and NHS to BSA-FITC were assessed at 25:75, 50:50, and 75:25, as shown in **Figure 2a** and **Figure S9**. Amongst all three conditions, when EDC/NHS was less than BSA-FITC, at a ratio of 25:75, the SNRs were significantly reduced across all dry times. This was expected, as less EDC/NHS to BSA-FITC resulted in overall reduced covalent crosslinking. The majority of the BSA-FITC were subsequently printed solely with physical immobilization through force application, and not all the BSA-FITC proteins were covalently crosslinked, making the cross-linking non-uniform. When EDC/NHS levels were higher than BSA-FITC levels in the bioink ratio 75:25, initial SNRs after 1min airdrying were the highest among the three conditions, but then significantly reduced when airdrying time increased. This is because EDC/NHS is highly reactive, and as such, having higher levels of EDC/NHS caused either protein aggregation or salt formation, when left to airdry longer than 1min. This is further shown in pockets with high

fluorescent intensities within each square at the longer airdrying times, indicative of the formation of circular aggregates (Figure S9). As highlighted in the FMEA, protein aggregation and salt formation from EDC/NHS reactivity are challenging to control. These issues lead to inconsistent fluorescence images, contributing to the high-risk RPN for the bioink formulation step of μCP. The %CVs for all conditions remained above 10% for inter-assay measurements, indicating non-repeatable and non-reproducible signals, which are unsuitable for industry applications (**Table S2**).

We also tested microcontact printing EDC/NHS separately, using a flat featureless stamp, before printing BSA-FITC, with a featured stamp. This could potentially decrease the chance of biomolecule aggregation in the bioink during the incubation time on the stamp. However, separate printing proved to be not as effective and required additional drying (**Figure S10**).

When optimizing the bioink formulation, understanding the effects of fluid flow during the droplet incubation and airdrying processes of μCP pointed to the use of an additive or agent within the bioink to prevent failure modes. In sessile droplets, after the application of the bioink to the stamp, the biomolecules tend to flow towards the periphery of the droplet due to surface tension gradients along the liquid-air interface, known as the Marangoni effect (**Figure 2b**).[66,67] This occurred whether higher or equal EDC/NHS to BSA-FITC were used. To assess how the Marangoni effect affects bioprinting and BSA-FITC immobilization after μCP, profilometry was conducted and surface topography was mapped on the printed substrate. As shown in the profilometry images (**Figure 2c** and **Figure S11**) and roughness profiles (**Figure S12**), the immobilized biomolecules accumulate along the edges, resulting in higher roughness values, with less biomolecules present in the center of the feature, known as a "coffee ring effect." By increasing viscosity, the Marangoni effect can be suppressed and the coffee ring effects minimized, for more uniform immobilization of biomolecules. [66–73]

Two additives of (3-Glycidyloxypropyl)trimethoxysilane (GLYMO) and glycerol were assessed for the optimization of the bioink formulation. GLYMO is an epoxy-based silane coupling reagent that can facilitate conjugation and chemical attachment of biomolecules to the surface through epoxy ring opening mechanism. However, in our experiment, epoxy showed reduced SNR of μCP microarrays, as it also prolonged the airdrying step (**Figure S13**) The increased wetness from the epoxy-based additive may stem from overly increasing the viscosity, resulting in a gel-like droplet, making the droplet removal step inconsistent. The extreme wetness prevented rapid airdrying of the droplet, making the μCP unsuitable for industry fabrication, which requires high speed, seamless and efficient production. This suggested that an alternative additive was needed to increase the viscosity of the bioink and reduce Maragoni effect, without increasing wetness or inducing highly gel-like bioink consistency.

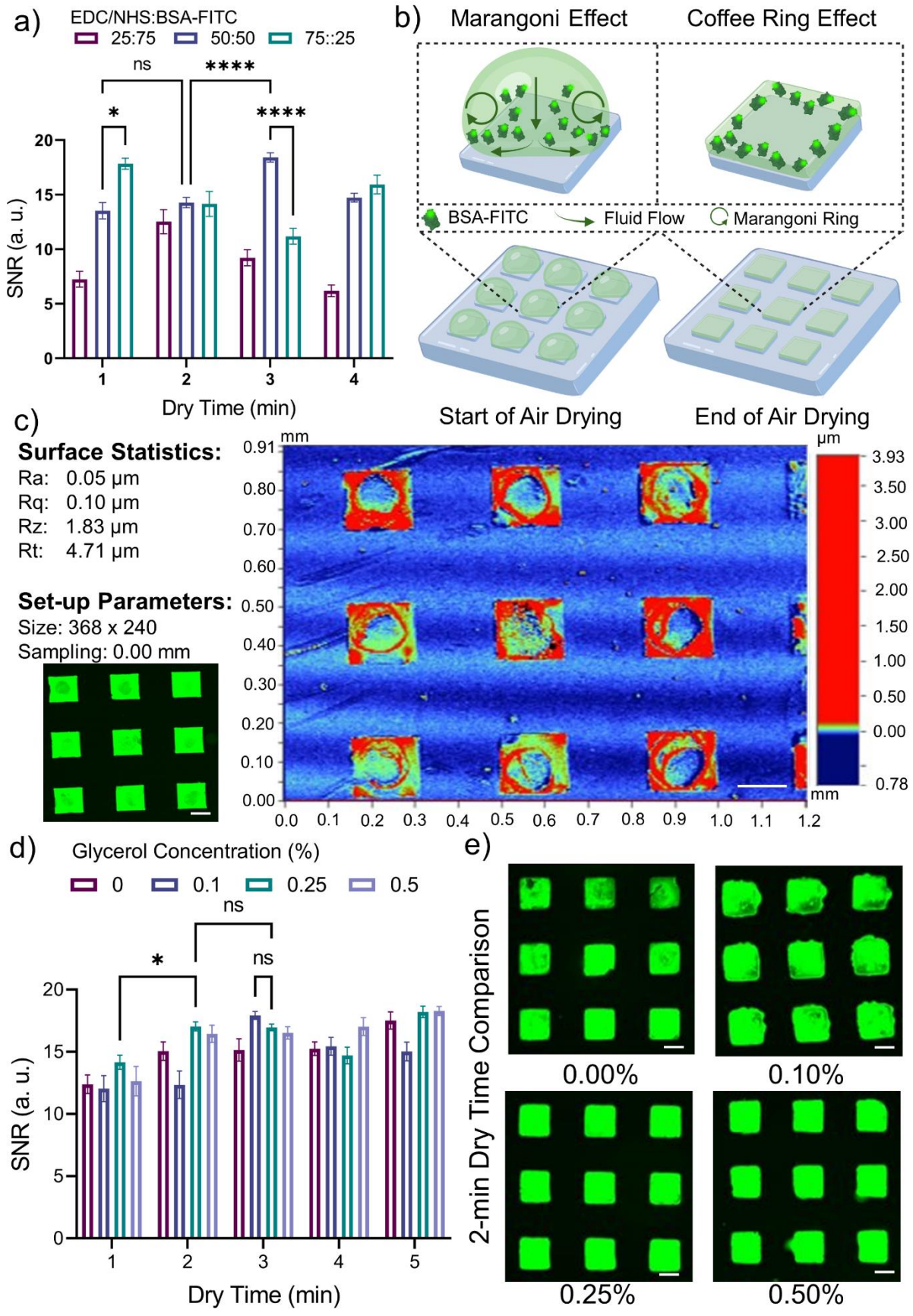

Figure 2. Optimization of Bioink Formulation. A) SNRs after µCP bioinks with EDC/NHS ratios of 25:75, 50:50, and 75:25, at dry times of 1 min, 2 min, 3 min and 4 min. **B)** Depicts the Marangoni Effect as stamps air dry, affecting the fluid flow and drying of bioink on individual stamp features, resulting in coffee ring effect. **C)** Profilometry profile depicting coffee ring effect on printed PMMA slides, with fluorescent image as comparison. **D)** SNRs after µCP bioinks with glycerol concentrations of 0%, 0.1%, 0.25% and 0.5% at dry times of 1 min, 2 min, 3 min, 4 min and 5 min. **E)** Fluorescence images of each glycerol concentration at 2 min dry time. Scale bars were 100 µm. Error bars calculated using standard error of the mean for all data.

Application of glycerol resulted in an increase of the SNR values. This could be attributed to the effect of glycerol in reducing Marangoni effects and air-drying times compared to GLYMO. Thus, glycerol showed more applicability in the µCP protocol for industrial fabrication as a more efficient and timelier bioink additive.[68,69,73] We further investigated the optimum concentration of glycerol in the bioink (**Figure 2d**). While the SNR values showed no significant difference amongst various glycerol concentrations, the 0.25% glycerol bioink, compared to the 0.1% glycerol bioink, showed lower %CV overall within the same print (intra-assay %CV), and between multiple prints (inter-assay %CV), indicating better repeatability and reproducibility. Specifically, the intra-assay %CVs were 8.81% and 13.58% for the 0.1% glycerol bioink, while for 0.25% glycerol bioinks, the intra-assay %CVs were 8.05% and 5.65%, after 3-min dry time. Meanwhile, the inter-assay %CVs were 11.19% and 6.85%, for the 0.1% and 0.25% glycerol bioinks, respectively (**Table S3**). These differences in %CV are visible in the fluorescent images of all glycerol bioinks, as the 0.25% glycerol bioink had consistent square shapes and low background noise (**Figure 2e and Figure S14)**.

When assessing the airdrying time, 1min airdrying showed significantly lower SNR results compared to 2min, indicating that the excess bioink was not sufficiently evaporated with a 1min airdrying time. The SNRs between 2min and 3min were not significantly different, requiring further assessment using %CVs. The inter-assay %CVs of 0.25% glycerol for the 2min and 3min airdrying were 12.77% and 6.85%, respectively (Table S3). The %CVs showed that 3min airdrying had higher repeatability and reproducibility, despite 2min and 3min conditions having similar SNR values. Through the assessment of glycerol, having uniform viscosity and fluid flow was essential for improving the immobilization of biomolecules throughout the printed substrates. The glycerol levels of 0.25% concentration, at 3min airdrying, was shown to have maximal SNR and minimal %CV.

Optimization of Droplet Removal, External Factors and Force Application

Three droplet removal strategies were assessed to determine the most effective method. These included wicking the droplet with a Kim-wipe, applying uniform centrifugal force for even droplet spreading, and removing the droplet at its edge. SNR and fluorescence images showed that pipette removal was the most accurate and precise droplet removal strategy, resulting in uniform and repeatable printed features (**Figure S15** and **Figure S16**). The CV values for droplet removal strategies also showed that pipette droplet removal had the lowest inter-assay %CV, of 8.22%, compared to Kim-wipe (51.36%) and centrifuge (42.08%) (**Table S4**).

Environmental factors, such as temperature and humidity control, play a key role in the airdrying protocol of our μCP process. Temperature and humidity have both been shown to affect the evaporation of drying sessile droplets.[73] As such, confining the stamps within a controlled environment and assessing the effects of temperature and relative humidity was performed. Increasing temperature resulted in significant SNR reduction, pointing to the role of temperature on droplet evaporation, as shown in **Figure S17.**

By controlling and increasing the environmental humidity to slow the evaporation rate, the consistency of the evaporation flux significantly improved compared to conditions with uncontrolled humidity, as outlined in **Figure 3a and 3b**. Various levels of controlled humidity were evaluated, with the highest SNR observed at 60% relative humidity for 3-min drying time (**Figure 3c and 3d**). However, there was no significant difference in SNR between 40% and 60% relative humidity for the same drying time. This suggests that the minimum humidity required to achieve SNR above 15 was 40%. At extreme humidity levels, such as 20% or 80%, the SNRs did not surpass 15. This outcome was likely due to the insufficient moisture at low humidity to establish an effective evaporation flux, or excessive moisture at high humidity, which hindered evaporation and prevented proper drying.

40% and 60% relative humidities were assessed for consistency at the 2-min and 3-min dry times to determine ideal environmental humidity **(Table S5).** The intra-assay %CVs of two wells for the 2-min dry time at 40% relative humidity were 4.60% and 16.45%, with the inter-assay %CV of 12.27%. In comparison, when increasing the dry time to 3-min, the intra-assay %CVs were reported as 16.17% and 7.41%, while the inter-assay %CV increased to 15.34%. The results showed that at 40% relative humidity, a 2-min drying time provided more consistency; however, with %CV values exceeding 10%, this condition was not suitable for achieving the industrial standards of repeatability and reproducibility. In comparison, 60% relative humidity at 3-min was able to achieve lower intra-assay %CVs of 9.25% and 11.13%, with an inter-assay %CV of 9.94%. This was also evident in the fluorescence images (Figure 3d and **Figure S18**), where 60% relative humidity had the nicest shaped squares and least visible background noise. The higher consistency, despite the longer dry time, makes 60% relative humidity at 3-min dry time the most repeatable and reproducible for industry applications. The longer drying time was due to the more balanced humidity environment, which created a uniform evaporation flux that slowed down compared to 40% relative humidity. Thus, 60% relative humidity and 3-min dry time was chosen as the optimized factors.

a)

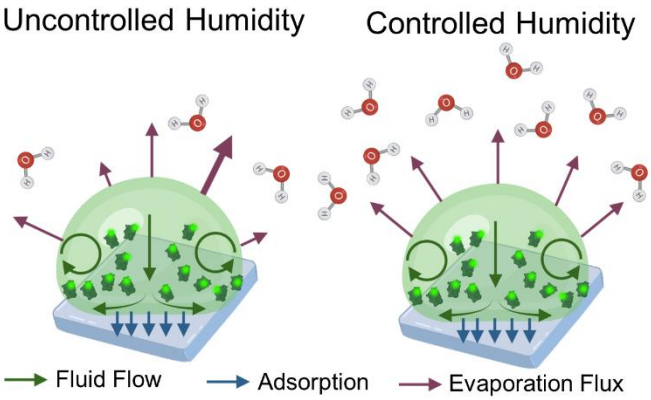

b)

Factor	Uncontrolled	Controlled
Moisture Level	Low Water Content	High Water Content
Evaporation Flux	Fast but Inconsistent	Slow but Consistent
Air Drying Time	Short but Inconsistent (High %CV)	Long but Consistent (Low %CV)

c)

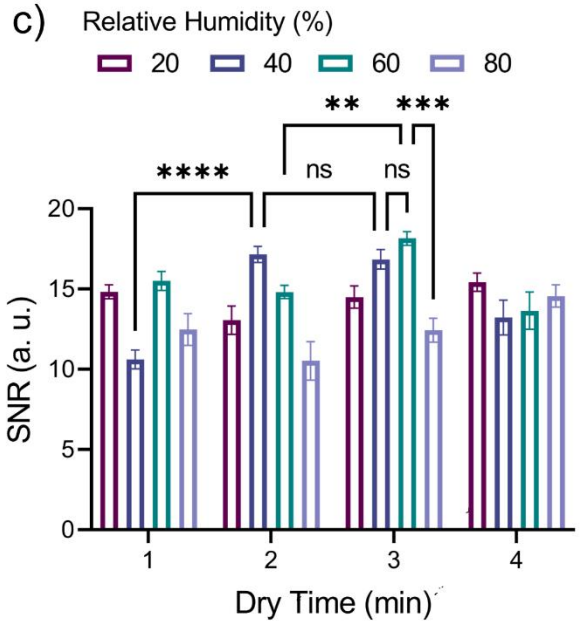

d)

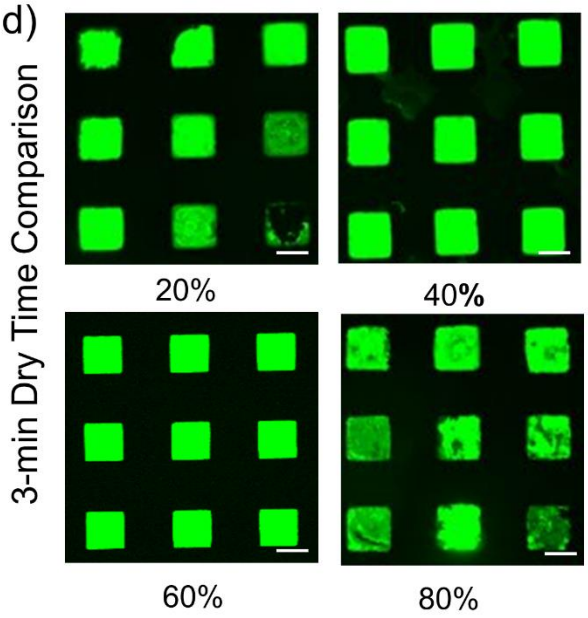

e)

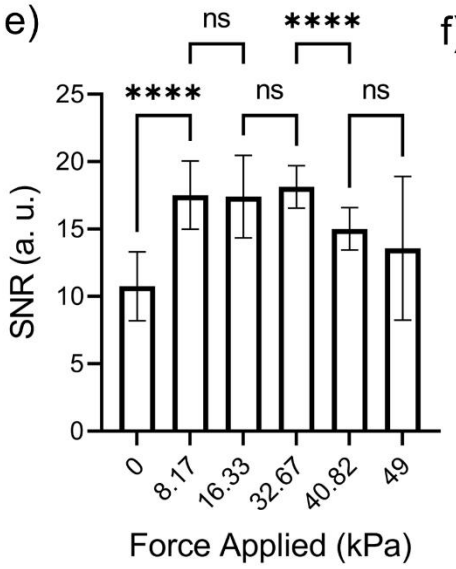

f)

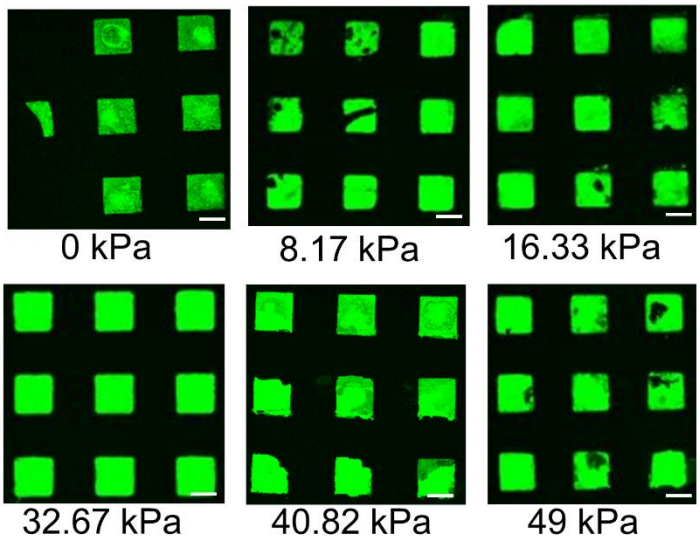

Figure 3. Optimization of external humidity and force application. A) Depicts the fluid flow, bioink adsorption and evaporation flux of bioink under uncontrolled and controlled humidity levels, during air drying on each stamp feature. **B)** A comparison of moisture level, evaporation flux and air-drying time between uncontrolled and controlled humidity environments. **C)** SNRs after μCP stamps under controlled relative humidity levels of 20%, 40%, 60% and 80%, at dry times of 1 min, 2 min, 3 min and 4 min. Error bars calculated using standard error of the mean. **D)** Fluorescence images of each relative humidity level at 3 min dry time. Scale bars were 100 μm. **E)** SNRs after μCP stamps using applied forces of 0 kPa, 8.17 kPa, 16.33 kPa, 32.67 kPa, 40.82 kPa, 49 kPa. Error bars calculated using the mean of standard deviation. **F)** Fluorescence images of each force applied with optimized bioink and external environment conditions. Scale bars were 100 μm.

The last step for optimization of the μCP protocol was determining the maximal force application for the highest bioink physical transfer and BSA-FITC immobilization. The assessment was done by application of 0 kPa and 49 kPa pressure on the stamps. The SNR values (**Figure 3e**) demonstrate that without force application (0 kPa), the SNR value was minimum. The SNR values significantly increased to values higher than 15 after the application of force. This determines that the force application ensures more effective physical bioink transfer from the stamp to the substrate. Inconsistencies of the %CVs also exist when no pressure is applied during the stamping process, at intra-assay %CVs of 31.04% and 14.01%, and inter-assay %CV of 23.75% (**Table S6**). The fluorescence images for 0kPa further depict the low bioink transfer (**Figure 3f**).

Among the pressures tested, the range of 8.17 to 32.67 kPa produced the highest SNRs, with no significant differences in SNR across this range (Figure 3e). Meanwhile, the %CV values were lowest when 32.67 kPa was applied, at intra-assay %CVs of 6.76% and 2.47%, as well as inter-assay %CVs of 4.99%. This shows that the value of 32.67 kPa was most repeatable and reproducible for industrial applications. Although 16.33 kPa resulted in intra-assay %CVs of 5.69% and 10.05%, and inter-assay %CVs of 8.91%, which are within acceptable industrial ranges for repeatability and reproducibility, 32.67 kPa demonstrated greater consistency overall, with lower %CVs. (Table S6). Additionally, among all the fluorescence images in Figure 3f, 32.67 kPa produced the most uniform and complete squares.

Exceeding 32.67 kPa resulted in a significant reduction in SNR. At these high pressures, stamps also experienced more buckling, higher damage to the PDMS features and higher occurrences of double printing. Additionally, the inter-assay values begin to increase and exceed the industrial threshold, reaching 10.48% and 27.65% for 40.82 kPa and 49 kPa, respectively (Table S6). While all squares were successfully printed, buckling of the stamp features caused visible holes in the fluorescence images in the fluorescence images, resulting in nonuniform fluorescence and increased inconsistency (Figure 3f).

Uniform Droplet Dispensing and Force Application for Preliminary Automation

Through industry standard FMEA analysis, we were able to pinpoint key risk factors and work towards a fully optimized and enhanced μCP process. Regardless, manual μCP limits the translation of μCP to industry scale manufacturing. Automation of μCP would allow for rapid high-throughput fabrication of lubricant-infused microarrays, making it possible to integrate with

current manufacturing machinery in industry.[74–76] To standardize the μCP protocol and to achieve industry-level scalability, we took the preliminary steps towards the automation of our optimized μCP protocol.

To automate the droplet addition and removal process, we developed a syringe pump operated mechanism. This system uses a 3D printed syringe apparatus connected to the pump via 1.5mm diameter tubing for precise droplet dispensing. As shown in **Figure 4a**, the syringe pump induced an automatic and consistent droplet dispensing and pick-up rate to standardize the speed of droplet application and removal. Furthermore, weight application was also standardized through the incorporation of an arbor press to allow for consistent force application, as seen in **Figure 4b.** 3D printing of a syringe apparatus and stamping mount allowed to fine tune the processes for the optimized bioink volumes, viscosity and stamp dimensions (**Figure 4c and 4d**).

Three conditions were tested in comparison to manual printing: 1) syringe pump only, with manual stamping conducted; 2) Arbor press only, with manual droplet application and removal; 3) a combined system of both syringe pump and arbor press. When compared to manual, as shown in **Figure 4e,** the combined system in which both syringe pump and arbor press were incorporated in the μCP protocol led to enhanced SNR with all optimized parameters. The %CV results shown in **Table S7** indicate that the combined automated system had the lowest %CVs, within industrial ranges, with intra-assay %CVs of 7.08% and 3.29%, and inter-assay %CV of 5.18%. Compared to manual printing, with intra-assay %CVs of 9.79% and 5.66%, as well as inter-assay %CV of 7.73%, the application of a fully automated system further reduced the inconsistency of μCP.

However, when only syringe pump for droplet addition and removal, or only the arbor press for force application, were used individually, the SNR was not enhanced as the failure modes identified in the FMEA remained possible. In fact, the SNRs were significantly reduced compared to manual printing, which could be due to the operator switching between manual and automated steps, prolonging the air-drying process between droplet removal and stamping (Figure 4e). When air-drying exceeded 3 minutes, as shown before, the SNR significantly decreased due to the over drying of the bioink, leading to inconsistencies in the final print. This was observed in the fluorescent images, where increased nonuniformity is observed in the printed squares of the syringe pump-only and arbor press-only conditions (Figure 4f). The high inter-assay values of 22.18% and 17.90%, for the syringe pump-only and arbor press-only, respectively, also depict the increase in inconsistency when relying on manual steps (Table S7).

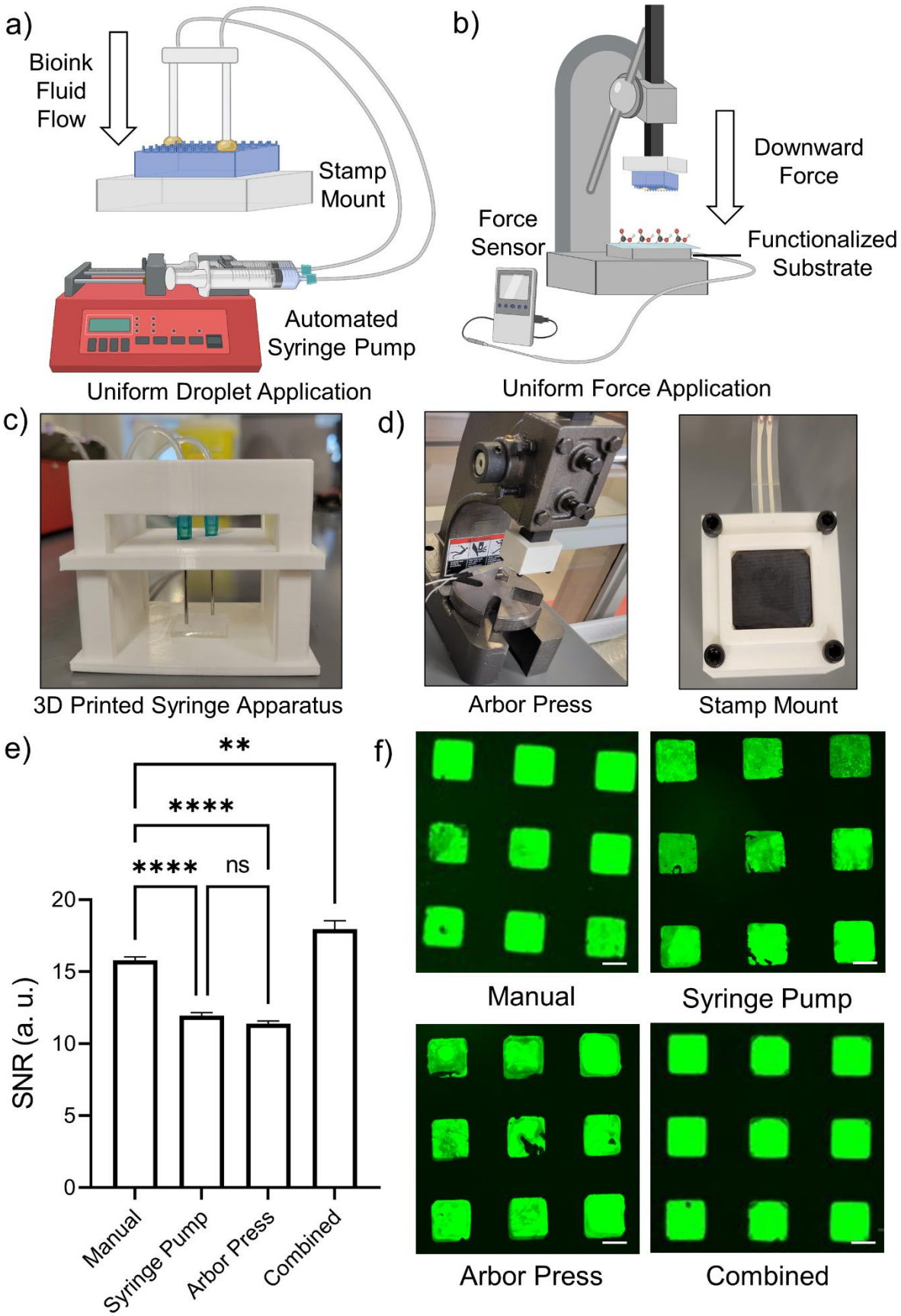

Figure 4. Depicts the standardization and preliminary automation steps of the optimized μCP protocol. A) Depicts the use of an automated syringe pump, stamp mount and syringe apparatus to control fluid flow upon droplet application and removal on the PDMS stamp. **B)** Depicts the use of an arbor press, with the PDMS stamp mount loaded for physical bioink transfer to the functionalized substrate. A standardized force sensor was incorporated to ensure the application of constant downward force. **C)** Shows the 3D printed syringe apparatus used for droplet application and removal. **D)** Shows the arbor press and 3D printed stamp mount for downward force application. **E)** SNRs after μCP stamps with optimized protocol conditions using manual printing, applying only the syringe pump, applying only the arbor press, and a combined syringe pump and arbor press set up. Error bars calculated using standard error of the mean. **F)** Florescence images of manual, syringe pump, arbor press, and combined set ups. Scale bars were 100 μm.

Future Outlook

In this work, we developed and optimized a μCP protocol using industrial risk assessment tools. [61–65] The use of a lubricant-infused surface provided a significant advantage by minimizing non-specific attachment, while incorporating a crosslinker enhanced the stability of biomolecule immobilization through covalent bonding. We established an optimized bioink ratio of 50:50 between crosslinker and biorecognition molecule. It was also determined that 0.25% glycerol is the most effective additive in reducing the highly common coffee ring effect, which significantly improved the SNRs of our printed lubricant-infused microarrays. Finally, environmental factors, such as temperature, relative humidity and force application were all optimized, at 20°C, 60% relative humidity and 32.67kPa, respectively.

From this optimized protocol, we developed a preliminary model for a proof-of-concept manufacturing process, using automated syringe pump droplet application and removal, as well as standardized arbor press and force sensor pressure application, with 3min airdrying in between. Regardless, as this is a preliminary prototype, key limitations exist in the design that will require iterative testing. These include having a streamlined connection between steps, where one step seamlessly integrates into the next, as in a product assembly line. As this prototype has only been tested in a laboratory setting, future steps of this work will be to conduct scaled up testing in industrial facilities.

To date, a fully optimized and standardized system for high-throughput μCP has not been reported for translating lab-scale processes to industrial manufacturing. Our proof-of-concept design addresses the key challenges of repeatability and reproducibility, marking a significant step toward automating μCP for large-scale production.

Experiential Method

Materials

The reagents and materials utilized for the experimental methods, such as surface functionalization, bioink formulation, and IFA preparation, include the following: SYLGARD^{TM} 184 Silicone Elastomer Base for Polydimethylsiloxane (PDMS) (Dow Silicones Corporation, Michigan, USA), SYLGARD^{TM} 184 Silicone Elastomer Curing Agent (Dow Silicones

Corporation, Michigan, USA), Poly(methyl methacrylate) (PMMA) (SQI Diagnostics, Etobicoke, ON, Canada), bovine serum albumin–fluorescein isothiocyanate conjugate (BSA-FITC) (Sigma-Aldrich, Oakville, ON, Canada), Glycerol, for molecular biology, ≥99% (Sigma-Aldrich, Oakville, ON, Canada), 1-Ethyl-3-(3-dimethylaminopropyl)carbodiimide (EDC) (Sigma-Aldrich, Oakville, ON, Canada), N-Hydroxysuccinimide, Solid, 98%, Poly bottle (NHS) (Sigma-Aldrich, Oakville, ON, Canada), (3-Glycidyloxypropyl)trimethoxysilane (GLYMO), print solution: 1X PBS + BSA + sugar (McMaster University, Hamilton, ON, Canada), Reconstitution Buffer 1 (PBS) (R&D Systems, Minnesota, USA), trichloro(1H,1H,2H,2H-perfluorooctyl) silane (TPFS) (Sigma-Aldrich, Oakville, ON, Canada), Perfluoroperhydrophenanthrene, selectophore™ (PFPP) (Sigma-Aldrich, Oakville, ON, Canada), biotinylated IL-6 monoclonal antibody (MQ2-39C3, anti-IL-6 DAb) (ThermoFisher Scientific, ON, Canada), human TNF RI/TNFRSF1A biotinylated antibody (anti-TNF-R1 DAb) (R&D Systems, Minnesota, USA), Streptavidin-Cy5 (Vector Laboratories, California, USA), Quantikine ELISA Wash Buffer (WB) (R&D Systems, Minnesota, USA), general assay diluent (ImmunoChemistry Technologies, California, USA).

Fabrication of PDMS Stamps

To fabricate the stamps, a pre-designed mold was created with the desired square pillar pattern. The square pillars had dimensions of 150μm width, 150μm length and 1μm height, with 'L' shaped landmarks to pinpoint specific areas for bioink application. The design was first modelled in Fusion 360, whereby a silicon mold with the predetermined design was fabricated utilizing photolithography. Afterwards, uncured PDMS was mixed with a PDMS curing agent at a ratio of 10:1 for 20 minutes *via* stirring. The mixture was then placed under vacuum in a desiccator at -0.08 MPa pressure for 45mins to allow for degassing of the mixture. The degassed mixture was poured into the silicon mold and heated for 24-hours at 60^{o}C, or until the mixture solidified. The stamps were removed from the mold and cut to dimensions of 1.8mm width, 2mm length and 1mm height. To clean the mold of debris, the stamps were sonicated for 5mins. The stamps were regularly imaged under brightfield using the Nikon ECLIPSE Ti2 Series Inverted Microscope to track the quality of the stamps overtime, and 10 uses was determined as the threshold of when the stamps became 'aged' stamps.

Substrate Preparation and Functionalization

Before functionalization, poly (methyl methacrylate) (PMMA) slides of dimensions 25mm x 29mm, were hand-washed with soap and DI water, carefully sprayed with 100% ethanol, and blow dried with nitrogen gas to remove any streaks or impurities. Then the PMMA slides were CO_2 – plasma treated for 15mins for the deposition of activated carboxyl groups using a PlasmaEtch PE-100. After functionalization, contact angle measurements using the Kruss Drop Shape Analyzer DSA30S were performed to assess the hydrophilicity of the functionalized PMMA.

Preparation of Bioink

The bioink used in this study was composed of the following: print solution (or PBS for control), glycerol, EDC/NHS and either BSA-FITC or DAb. First GLYMO epoxy or glycerol was serially diluted in print solution or PBS. Then EDC was measured at 5mg (± 0.3mg) and NHS was measured at 3mg (± 0.3mg). The EDC/NHS combination was then dissolved in solution of glycerol

and print solution. After each of the mentioned steps, the solutions were mixed *via* vortex at maximum speed for 10-20 seconds. Finally, the EDC/NHS solution was mixed with BSA-FITC, also diluted in print solution, with a stock concentration of 3mg/mL during the optimization tests. For anti-IL-6 and/or anti-TNF RI DAb, they were prepared at a concentration of 200µg/mL. The final solution, containing either BSA-FITC or DAb was mixed *via* pipette. In the separate printing test, EDC/NHS and BSA-FITC were not mixed in this method, but individually printed, either immediately after one another or with a 1min, 2min, 3min or 4min incubation between separate prints.

Immobilization of Biomolecules Through µCP

The bioink was applied to each PDMS stamp within the 'L' shape of the two landmark regions at 5µL volume per droplet, applied manually *via* pipette. The droplets incubated for 2mins to allow for the bioink to be absorbed into the PDMS pillar shapes, before removal with pipette, Kim-wipe or centrifugal force. The excess bioink was air dried in which during optimization and air-drying times were assessed at different controlled humidity environments. After air drying, the stamp was flipped and placed on the functionalized PMMA substrate, and a weight was manually applied to facilitate physical transfer of the bioink from the PDMS stamp to the PMMA substrate. After 1min of weight application, the weight and stamp were removed, and the PMMA substrates incubated in a controlled ~100% relative humidity environment for 1-hour. Chemical vapour deposition (CVD) using TPFS was then performed for 15mins to allow for fluorosilanization of the printed PMMA substrates. Wells were created on the substrates using a 16-well superstructure assembly, whereby PFPP lubricant was applied, and three consecutive 10min washes were conducted, in controlled relative humidity of ~100%.

Profilometry

A Wyko NT1100 Profilometer was utilized for mapping the surface roughness of the printed substrates. The system was calibrated with a modulation threshold of 3%, at vertical scanning interferometry (VSI) mode. The parameters set were at 368 X 240mm window size for imaging all 9 squares, with 0.00 mm sampling. Images were taken at 5X objective, and X/Y profile graphs as well as 3-D projections were acquired.

SNR and CV Calculations

A Nikon ECLIPSE Ti2 Series Inverted Microscope was utilized for imaging of the results. Afterwards, ImageJ software was utilized to quantify the signal and relative background noise of 9 individual square replicates for each well printed. The signal-to-noise ratio (SNR) of each square was calculated by dividing signal over noise, and a mean average was calculated amongst all 9 squares, or replicates, referred to as the intra-assay SNR. Averages were taken of the intra-assay SNR for all wells printed from each stamp to determine the inter-assay SNR. Similarly, an intra-assay percent coefficient of variance (%CV) was calculated for each well, which had 9 replicates each, and the inter-assay %CV was quantified by calculated %CV amongst all wells from a single stamp. **Equation 1** was utilized for the calculation of these %CVs. Statistical analysis was conducted for each condition where SNR was calculated and was tested using 2-way ANOVA (or mixed effects analysis with Geiser – Greenhouse corrections), where nonsignificant (ns) statistical

values, P = 0.5, and 1-star showing significance with P<0.1, 3-star with P <0.001 and 4-star with P<0.0001.

1) $\%CV = \frac{standard\ deviation\ of\ each\ SNR\ value}{average\ SNR}(100\%)$

Optimization of Protocol Utilizing BSA-FITC

To optimize the μCP protocol, a failure mode and effects analysis (FMEA) was utilized to assess the risk of failure at each experimental step. Each step was evaluated based on severity of the failure in impacting the results, the frequency of failure occurrence, and the difficulty of detecting failure upon occurrence, by which the product of these factors determined the overall risk priority number (RPN). Optimization of BSA-FITC targeted the high-risk steps in the protocol determined by the FMEA. For the bioink preparation, concentrations of glycerol, EDC/NHS and BSA-FITC were assessed. 0%, 0.1%, 0.25% and 0.5% glycerol concentrations, as well as EDC values of 4.5mg, 5mg and 5.5mg, and NHS values of 2.5mg, 3mg, and 3.5mg, were all assessed as contents of the bioink. The ratio of EDC/NHS: BSA-FITC solution was also varied by ratios of 75:25, 50:50 and 25:75, to determine ideal ratio for chemical crosslinking and attachment. For removal of droplets, pipette removal was assessed compared to Kim-wipe and centrifuge removal. Finally, for air drying step, various dry times were assessed, including 1min, 2min, 3min, and 4min at different humidity-controlled environment conditions of 20%, 40%, 60% and 80%. Furthermore, weight application after air drying and amount of weight, between 0 – 1.5kg, were also assessed to determine ideal amount of force for physical bioink transfer. These weights were converted from kg to kPa using **Equation 2**. Fluorescence microscopy was conducted under FITC at exposure 300ms for LUTs of 100-350. SNR, statistical analyses and CVs were also calculated for each optimization.

2) $Pressure\ Applied\ (kPA) = \frac{Weight\ (kg) * 9.8\frac{m}{s^2}}{Area\ of\ Stamp * 1000}$

Automation and Standardization of μCP Protocol

Automation of the μCP process focused on the droplet application and removal process as well as the force application process. First, a droplet application dispensing mechanism was modelled in Fusion 360 3-D modelling software, and 3-D printed with resin using the B9 Core 530 3D Printer. The outer diameter for the droplet dispensing apparatus was 2.5mm, and the inner syringe diameter was 1.5mm, with 1mm thick walls. The apparatus was connected to a NE-1600 Six Channel Programmable Syringe Pump *via* tubing. Through this method, the syringe pump was programmed to dispense and pick up 5μL of bioink, replacing the pipette in the manual method. Furthermore, a 0.5 Inch Dia FSR402 Resistive Thin Film Pressure Sensor (Force Sensing Resistor 0-10kg) and Arduino Uno R3 were utilized to measure the exact force application placed on each stamp. This force sensor was connected to a HHIP 8600-0031 Heavy Duty Arbor Press (0.5-ton capacity, 10" height) to standardize the method of force application to prevent double printing of the stamp, which can occur in the manual protocol.

Acknowledgements

This research was undertaken, in part, thanks for Canada Research Chairs Program to T.F. Didar. T.F. Didar is funded by the Natural Sciences and Engineering Research Council (NSERC) through the Canada Discovery Grant, Ontario Early Researcher Award and Collaborative Research and Development Grant.

Works Cited

[1] D. Bisht, S. Saxena, N. S. Kharayat, S. Gautam, **2022**, pp. 215–229.

[2] Z. Matharu, O. Polat, in *Advances in Personalized Nanotherapeutics*, Springer International Publishing, Cham, **2017**, pp. 217–230.

[3] A. Mobed, S. K. Shakouri, S. Dolati, *Cytokine* **2020**, *136*, 155272.

[4] A. van Belkum, C. Almeida, B. Bardiaux, S. V. Barrass, S. J. Butcher, T. Çaykara, S. Chowdhury, R. Datar, I. Eastwood, A. Goldman, M. Goyal, L. Happonen, N. Izadi-Pruneyre, T. Jacobsen, P. H. Johnson, V. A. J. Kempf, A. Kiessling, J. L. Bueno, A. Malik, J. Malmström, I. Meuskens, P. A. Milner, M. Nilges, N. Pamme, S. A. Peyman, L. R. Rodrigues, P. Rodriguez-Mateos, M. G. Sande, C. J. Silva, A. C. Stasiak, T. Stehle, A. Thibau, D. J. Vaca, D. Linke, *Diagnostics* **2021**, *11*, 1259.

[5] N. Dutta, P. B. Lillehoj, P. Estrela, G. Dutta, *Biosensors (Basel)* **2021**, *11*, 94.

[6] J. Su, S. Chen, Y. Dou, Z. Zhao, X. Jia, X. Ding, S. Song, *Anal Chem* **2022**, *94*, 3235.

[7] E. Cecon, A. Oishi, M. Luka, D. Ndiaye-Lobry, A. François, M. Lescuyer, F. Panayi, J. Dam, P. Machado, R. Jockers, *Elife* **2023**, *12*, DOI 10.7554/eLife.78360.

[8] A. Shakeri, N. A. Jarad, J. Terryberry, S. Khan, A. Leung, S. Chen, T. F. Didar, *Small* **2020**, *16*, 2003844.

[9] H. Yousefi, H. Su, M. Ali, C. D. M. Filipe, T. F. Didar, *Adv Mater Interfaces* **2018**, *5*, DOI 10.1002/admi.201800659.

[10] S. Al Abdullah, L. Najm, L. Ladouceur, F. Ebrahimi, A. Shakeri, N. Al-Jabouri, T. F. Didar, K. Dellinger, *Adv Funct Mater* **2023**, *33*, DOI 10.1002/adfm.202302673.

[11] A. Prasad, S. Khan, J. K. Monteiro, J. Li, F. Arshad, L. Ladouceur, L. Tian, A. Shakeri, C. D. M. Filipe, Y. Li, T. F. Didar, *Advanced Materials* **2023**, *35*, DOI 10.1002/adma.202302641.

[12] V. Romanov, B. D. Brooks, **2021**, pp. 151–177.

[13] T. F. Didar, K. Li, T. Veres, M. Tabrizian, *Biomaterials* **2013**, *34*, 5588.

[14] T. F. Didar, M. Tabrizian, *Lab Chip* **2012**, *12*, 4363.

[15] T. F. Didar, K. Li, M. Tabrizian, T. Veres, *Lab Chip* **2013**, *13*, 2615.

[16] P. Ihalainen, A. Määttänen, N. Sandler, *Int J Pharm* **2015**, *494*, 585.

[17] S. Park, H. Kim, J.-H. Kim, W.-H. Yeo, *Materials* **2020**, *13*, 3587.

[18] A. J. Summers, J. P. Devadhasan, J. Gu, D. C. Montgomery, B. Fischer, M. A. Gates-Hollingsworth, K. J. Pflughoeft, T. Vo-Dinh, D. P. AuCoin, F. Zenhausern, *ACS Omega* **2022**, *7*, 32262.

[19] S. ILKHANIZADEH, A. TEIXEIRA, O. HERMANSON, *Biomaterials* **2007**, *28*, 3936.

[20] L. Tian, L. He, K. Jackson, A. Saif, S. Khan, Z. Wan, T. F. Didar, Z. Hosseinidoust, *Nat Commun* **2022**, *13*, 7158.

[21] A. Perl, D. N. Reinhoudt, J. Huskens, *Advanced Materials* **2009**, *21*, 2257.

[22] A. Garcia-Cruz, M. Lee, N. Zine, M. Sigaud, P. Marote, M. Lopez, J. Bausells, N. Jaffrezic-Renault, A. Errachid, *Materials Science and Engineering: C* **2018**, *91*, 466.

[23] S. Qiu, J. Ji, W. Sun, J. Pei, J. He, Y. Li, J. J. Li, G. Wang, *Smart Mater Med* **2021**, *2*, 65.

[24] S. Alom Ruiz, C. S. Chen, *Soft Matter* **2007**, *3*, 168.

[25] A. Shakeri, S. Khan, T. F. Didar, *Lab Chip* **2021**, *21*, 3053.

[26] T. Kaufmann, B. J. Ravoo, *Polym Chem* **2010**, *1*, 371.

[27] A. Shakeri, N. A. Jarad, S. Khan, T. F Didar, *Anal Chim Acta* **2022**, *1209*, 339283.

[28] J. Peng, D. Zhao, X. Tang, F. Tong, L. Guan, Y. Wang, M. Zhang, T. Cao, *Langmuir* **2013**, *29*, 11809.

[29] A. J. Khadpekar, M. Khan, A. Sose, A. Majumder, *Sci Rep* **2019**, *9*, 1024.

[30] K. Willson, A. Atala, J. J. Yoo, *Biomolecules* **2021**, *11*, 1593.

[31] A. Shakeri, S. M. Imani, E. Chen, H. Yousefi, R. Shabbir, T. F. Didar, *Lab Chip* **2019**, *19*, 3104.

[32] A. Gharia, E. P. Papageorgiou, S. Giverts, C. Park, M. Anwar, *Mol Imaging* **2020**, *19*, 1536012120913693.

[33] J. Philip, K. Carlsson, *Journal of the Optical Society of America A* **2003**, *20*, 368.

[34] H. Wang, X. Feng, B. Shi, W. Liang, Y. Chen, J. Wang, X. Li, *Rev Sci Instrum* **2018**, *89*, 093114.

[35] Z. He, J. Zhou, *Appl Environ Microbiol* **2008**, *74*, 2957.

[36] X. Liu, H. Zhu, J. Sabó, Z. Lánský, P. Neužil, *Sci Rep* **2022**, *12*, 18911.

[37] "Signal-to-Noise Ratio (SNR)," can be found under https://svi.nl/Signal-to-Noise-Ratio, **2024**.

[38] A. Kumar, S. Sankalp, R. Remesan, **2023**, pp. 1–15.

[39] S. Khan, A. Shakeri, J. K. Monteiro, S. Tariq, A. Prasad, J. Gu, C. D. M. Filipe, Y. Li, T. F. Didar, *Sci Rep* **2024**, *14*, 8277.

[40] L. Lunelli, F. Barbaresco, G. Scordo, C. Potrich, L. Vanzetti, S. L. Marasso, M. Cocuzza, C. F. Pirri, C. Pederzolli, *Applied Sciences* **2020**, *10*, 3867.

[41] R. T. Aggarwal, L. Lai, H. Li, *Anal Biochem* **2023**, *683*, 115369.

[42] H. Lee, D. Koh, L. Xu, S. Row, S. T. Andreadis, K. W. Oh, *Micromachines (Basel)* **2016**, *7*, DOI 10.3390/mi7100173.

[43] V. A. Bot, A. Shakeri, J. I. Weitz, T. F. Didar, *Adv Funct Mater* **2022**, *32*, DOI 10.1002/adfm.202205078.

[44] C. Matellan, A. E. del Río Hernández, *Sci Rep* **2018**, *8*, 6971.

[45] A. Shakeri, H. Yousefi, N. A. Jarad, S. Kullab, D. Al-Mfarej, M. Rottman, T. F. Didar, *Sci Rep* **2022**, *12*, 14486.

[46] T. Didar, A. Shakeri, H. Yousefi, *Lubricant-Infused Surface Biosensing Interface, Methods of Making and Uses Thereof*, **2021**, US20230349893A1.

[47] H. Yousefi, S. E. Samani, S. Khan, A. Prasad, A. Shakeri, Y. Li, C. D. M. Filipe, T. F. Didar, *ACS Nano* **2022**, *16*, 29.

[48] E. Kasapgil, M. Badv, C. A. Cantú, S. Rahmani, H. Y. Erbil, I. Anac Sakir, J. I. Weitz, Z. Hosseini-Doust, T. F. Didar, *ACS Biomater Sci Eng* **2021**, *7*, 541.

[49] M. Villegas, Y. Zhang, M. Badv, C. Alonso-Cantu, D. Wilson, Z. Hosseinidoust, T. F. Didar, *Sci Rep* **2022**, *12*, 5380.

[50] S. Khan, N. A. Jarad, L. Ladouceur, K. Rachwalski, V. Bot, A. Shakeri, R. Maclachlan, S. Sakib, J. I. Weitz, E. D. Brown, L. Soleymani, T. F. Didar, *Small* **2022**, *18*, DOI 10.1002/smll.202108112.

[51] E. Afonso, F. Bayat, L. Ladouceur, S. Khan, A. Martínez-Gómez, J. I. Weitz, Z. Hosseinidoust, P. Tiemblo, N. García, T. F. Didar, *ACS Appl Mater Interfaces* **2022**, *14*, 53535.

[52] N. Abu Jarad, K. Rachwalski, F. Bayat, S. Khan, A. Shakeri, R. MacLachlan, M. Villegas, E. D. Brown, L. Soleymani, T. F. Didar, *Small* **2023**, *19*, DOI 10.1002/smll.202205761.

[53] N. Abu Jarad, K. Rachwalski, F. Bayat, S. Khan, A. Shakeri, R. MacLachlan, M. Villegas, E. D. Brown, Z. Hosseinidoust, T. F. Didar, L. Soleymani, *ACS Appl Mater Interfaces* **2023**, *15*, 16253.

[54] R. MacLachlan, F. Kanji, S. Sakib, S. Khan, C. Pattyn, S. M. Imani, T. F. Didar, L. Soleymani, *ACS Appl Mater Interfaces* **2023**, *15*, 55287.

[55] S. Khan, B. Burciu, C. D. M. Filipe, Y. Li, K. Dellinger, T. F. Didar, *ACS Nano* **2021**, *15*, 13943.

[56] H. Puliyalil, U. Cvelbar, *Nanomaterials (Basel)* **2016**, *6*, DOI 10.3390/nano6060108.

[57] M. Fleischer, Z. Kelar Tučeková, O. Galmiz, E. Baťková, T. Plšek, T. Kolářová, D. Kováčik, J. Kelar, *Nanomaterials* **2024**, *14*, 426.

[58] A. Shakeri, N. A. Jarad, A. Leung, L. Soleymani, T. F. Didar, *Adv Mater Interfaces* **2019**, *6*, DOI 10.1002/admi.201900940.

[59] S. M. Imani, M. Badv, A. Shakeri, H. Yousefi, D. Yip, C. Fine, T. F. Didar, *Lab Chip* **2019**, *19*, 3228.

[60] J. H. L. Beal, A. Bubendorfer, T. Kemmitt, I. Hoek, W. Mike Arnold, *Biomicrofluidics* **2012**, *6*, 36503.

[61] M. Gul, M. Yucesan, E. Celik, *Appl Soft Comput* **2020**, *96*, 106689.

[62] J. Huang, J.-X. You, H.-C. Liu, M.-S. Song, *Reliab Eng Syst Saf* **2020**, *199*, 106885.

[63] K. A. Nealon, P. A. Balter, R. J. Douglas, D. K. Fullen, P. L. Nitsch, A. M. Olanrewaju, M. Soliman, L. E. Court, *Pract Radiat Oncol* **2022**, *12*, e344.

[64] A. Mascia, A. M. Cirafici, A. Bongiovanni, G. Colotti, G. Lacerra, M. Di Carlo, F. A. Digilio, G. L. Liguori, A. Lanati, A. Kisslinger, *Accreditation and Quality Assurance* **2020**, *25*, 311.

[65] J. A. L. Anjalee, V. Rutter, N. R. Samaranayake, *BMC Public Health* **2021**, *21*, 1430.

[66] C. Yang, Z.-S. Mao, in *Numerical Simulation of Multiphase Reactors with Continuous Liquid Phase*, Elsevier, **2014**, pp. 5–73.

[67] A. Hooshanginejad, S. Jung, *Symmetry (Basel)* **2022**, *14*, 425.

[68] L. Thayyil Raju, C. Diddens, Y. Li, A. Marin, M. N. van der Linden, X. Zhang, D. Lohse, *Langmuir* **2022**, *38*, 12082.

[69] K. Takamura, H. Fischer, N. R. Morrow, *J Pet Sci Eng* **2012**, *98–99*, 50.

[70] N. Jung, H. W. Seo, P. H. Leo, J. Kim, P. Kim, C. S. Yoo, *Soft Matter* **2017**, *13*, 6529.

[71] J.-C. Baret, *Lab Chip* **2012**, *12*, 422.

[72] C. Seo, D. Jang, J. Chae, S. Shin, *Sci Rep* **2017**, *7*, 500.

[73] B. Yang, M. M. Sarafraz, M. Arjomandi, *Appl Therm Eng* **2019**, *161*, 114142.

[74] M.-N. Doulgkeroglou, A. Di Nubila, B. Niessing, N. König, R. H. Schmitt, J. Damen, S. J. Szilvassy, W. Chang, L. Csontos, S. Louis, P. Kugelmeier, V. Ronfard, Y. Bayon, D. I. Zeugolis, *Front Bioeng Biotechnol* **2020**, *8*, DOI 10.3389/fbioe.2020.00811.

[75] P. Alavian, Y. Eun, S. M. Meerkov, L. Zhang, *Int J Prod Res* **2020**, *58*, 828.

[76] Y. Lu, X. Xu, L. Wang, *J Manuf Syst* **2020**, *56*, 312.